Unraveling Kinetically-Driven Mechanisms of Gold Nanocrystal Shape Transformations using Graphene Liquid Cell Electron Microscopy

Matthew R. Hauwiller[†], Layne B. Frechette[†‡], Matthew R. Jones[†], Justin C. Ondry[†], Grant M. Rotskoff[¶], Phillip Geissler[†], and A. Paul Alivisatos[†§⊥‖]*

† Department of Chemistry, University of California-Berkeley, Berkeley, CA, United States, 94720.

§ Department of Materials Science and Engineering, University of California-Berkeley, Berkeley, CA, United States, 94720.

¶ Courant Institute of Mathematical Sciences, New York University, New York, United States, 10012.

‡ Erwin Schrödinger Institute for Mathematics and Physics, University of Vienna, Austria, 1090.

⊥ Materials Sciences Division, Lawrence Berkeley National Laboratory, Berkeley, CA, United States, 94720.

‖ Kavli Energy NanoScience Institute, University of California-Berkeley and Lawrence Berkeley National Laboratory, Berkeley, CA, United States, 94720.

*E-mail: paul.alivisatos@berkeley.edu

TOC FIGURE
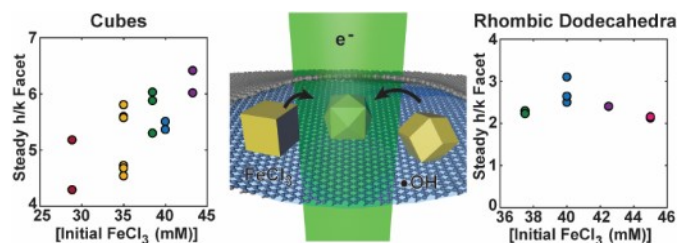
ABSTRACT

Mechanisms of kinetically-driven nanocrystal shape transformations were elucidated by monitoring single particle etching of gold nanocrystals using *in situ* Graphene Liquid Cell TEM. By systematically changing the chemical potential of the oxidative etching and then quantifying the facets of the nanocrystals, non-equilibrium processes of atom removal could be deduced. Etching at sufficiently high oxidation potentials, both cube and rhombic dodecahedra (RDD)-shaped gold nanocrystals transform into kinetically-stable tetrahexahedra (THH)-shaped particles. Whereas {100}-faceted cubes adopt an {hk0}-faceted THH intermediate where h/k depends on chemical potential, {110}-faceted RDD adopt a {210}-faceted THH intermediate regardless of driving force. For cube reactions, Monte Carlo simulations show that removing 6-coordinate edge atoms immediately reveals 7-coordinate interior atoms. The rate at which these 6- and 7-coordinate atoms are etched is sensitive to the chemical potential, resulting in different THH facet structures with varying driving force. Conversely, when RDD are etched to THH, removal of 6-coordinate edge atoms reveals 6-coordinate interior

atoms. Thus, changing the driving force for oxidation does not change the probability of edge atom versus interior atom removal, leading to a negligible effect on the kinetically-stabilized intermediate shape. These fundamental insights, facilitated by single-particle liquid-phase TEM imaging, provide important atomic-scale mechanistic details regarding the role of kinetics and chemical driving force in dictating shape transformations at the nanometer length scale.
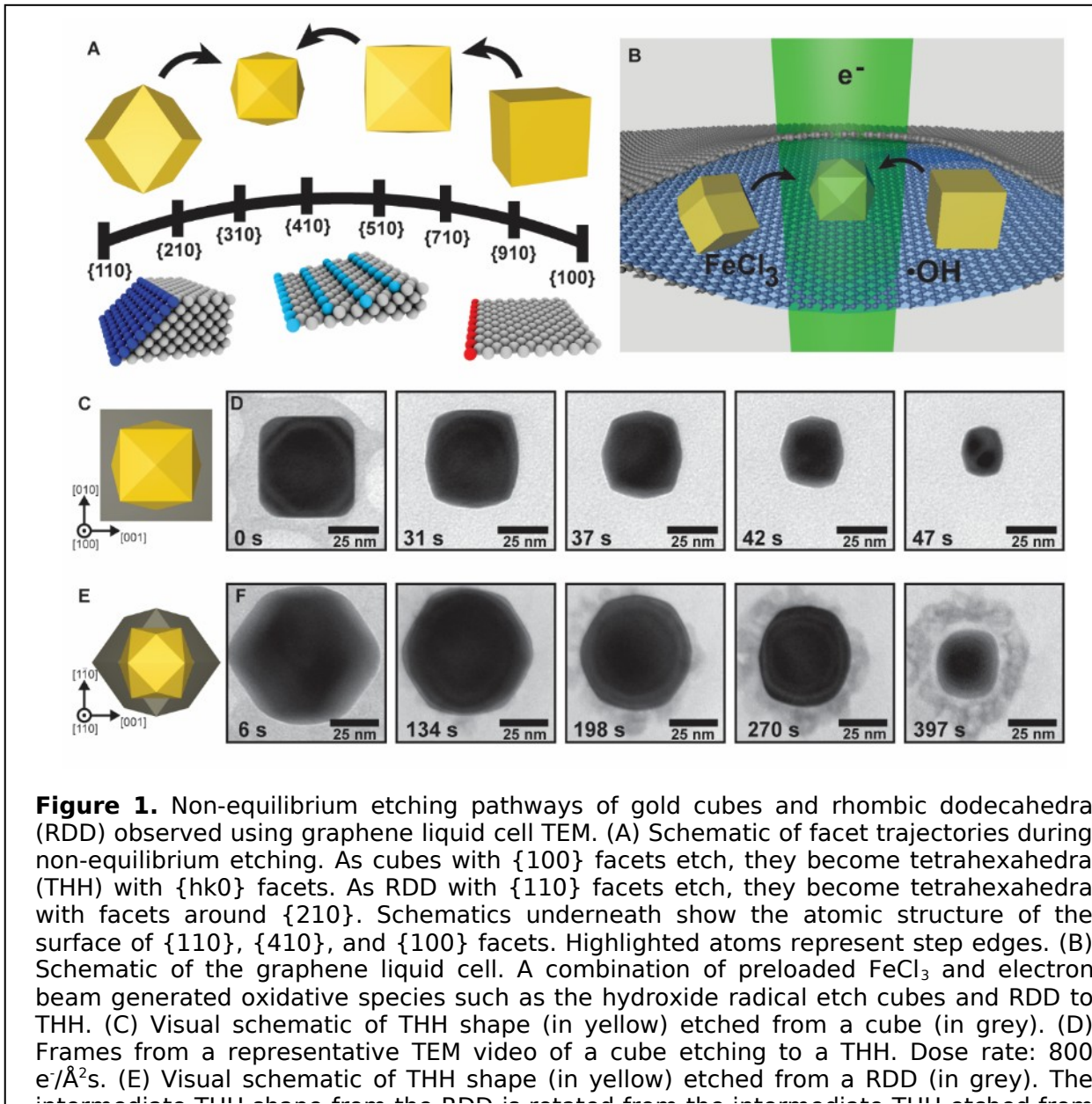
KEYWORDS

Graphene Liquid Cell, TEM, nanocrystals, oxidative etching

TEXT

Understanding and controlling how atoms are organized to form larger structures during crystal synthesis is a fundamental goal of nanochemistry. This is due, in part, to the drive to tune the size, shape, and exposed facets of a nanoparticle to program its optical,[1,2] catalytic,[3,4] and biomedical properties.[5-7] Kinetically-driven syntheses are particularly appealing as they can yield nanocrystals with high-index facets and exotic structures.[8-10] However, the mechanisms underlying many of these non-equilibrium reactions are poorly understood and difficult to probe experimentally. With a better understanding of non-equilibrium processes in nanoscale systems, chemists can improve their ability to controllably make energetically unfavorable nanocrystals with tailored facets and properties.[11,12]

Liquid cell transmission electron microscopy (TEM) is an appealing technique for probing kinetically-dominated nanocrystal reactions as it allows for direct imaging of dynamics and structural transformations at the single particle level in a liquid environment.[13-17] Encapsulating the liquid solution between sheets of atomically-thin graphene provides exceptional spatial resolution for investigating nanocrystal facet and atomic dynamics.[18-21] Liquid cell TEM can provide mechanistic information about nanocrystal etching on the single particle level,[22-24] and recent work by our group has demonstrated the ability to etch gold nanocrystals in graphene liquid cells, revealing the presence of high-energy intermediate shapes during a kinetically controlled reaction.[25] Here, we explore the effects of the chemical potential used to drive the etching process. Control of the driving force and the extent to which the system is kinetically controlled provides new insights into the transformation pathways of non-equilibrium nanoparticle formation reactions.

In this work, we modulate the oxidation potential in Graphene Liquid Cell nanoparticle etching reactions by changing the concentration of a chemical etchant ($FeCl_3$) while holding constant the electron beam dose rate. Whereas cubic nanocrystals were observed to transform into tetrahexahedra intermediates with different {hk0} crystal facets depending on the chemical potential ($FeCl_3$ concentration), rhombic dodecahedra nanocrystals transformed into the same tetrahexahedra intermediate, regardless of chemical potential. Monte Carlo simulations and zero temperature kinetic models were used to elucidate the underlying mechanisms by which

Figure 1. Non-equilibrium etching pathways of gold cubes and rhombic dodecahedra (RDD) observed using graphene liquid cell TEM. (A) Schematic of facet trajectories during non-equilibrium etching. As cubes with {100} facets etch, they become tetrahexahedra (THH) with {hk0} facets. As RDD with {110} facets etch, they become tetrahexahedra with facets around {210}. Schematics underneath show the atomic structure of the surface of {110}, {410}, and {100} facets. Highlighted atoms represent step edges. (B) Schematic of the graphene liquid cell. A combination of preloaded $FeCl_3$ and electron beam generated oxidative species such as the hydroxide radical etch cubes and RDD to THH. (C) Visual schematic of THH shape (in yellow) etched from a cube (in grey). (D) Frames from a representative TEM video of a cube etching to a THH. Dose rate: 800 $e^-/Å^2s$. (E) Visual schematic of THH shape (in yellow) etched from a RDD (in grey). The intermediate THH shape from the RDD is rotated from the intermediate THH etched from

chemical driving force controls which atoms are removed and what non-equilibrium facets are formed.

In all experiments, gold nanocrystals[26] are suspended in aqueous solutions of $FeCl_3$ and Tris Buffer-HCl and encapsulated in a graphene liquid cell[21] (nanocrystal synthesis and graphene liquid cell methods are in the

Supporting Information). These conditions allow for non-equilibrium particle etching to occur in the presence of the electron beam via a combination of the oxidative species generated locally as byproducts of radiolysis[27,28] and the $FeCl_3$.[29-31] For all non-equilibrium etching conditions, gold cubes and RDD transition into tetrahexahedra (THH) shapes (Figure 1A). The cube and RDD are composed of high symmetry {100} and {110} surface facets, respectively, while the THH are composed of {hk0} surface facets. High index {hk0} facets are vicinal facets composed of {100} terraces separated by steps (Figure 1A). The h/k value of an {hk0} facet describes the atomic width of each {100} terrace, and the vicinal angle is defined as the angle between a {100} surface and the {hk0} surface. Cubes can be thought of as an infinitely long {100} terrace (h/k → ∞), while the {110} RDD are the limit where each terrace is only a single atom wide (h/k = 1). Therefore, a continuous hypothetical transformation from a cube to a THH to an RDD is possible by decreasing the size of the {100} terraces of the surface facets of the initial nanocrystal. From a shape perspective, the {hk0} THH can be thought of as cubes with pyramids on each face, with the angle of each pyramid corresponding to the vicinal angle of the {hk0} facet. When visually comparing the intermediate THH shapes generated by etching the cubes and RDD (Figure 1B), the THH appear rotated because the cubes are oriented along the [100] zone axis, and the RDD are oriented along the [110] zone axis (Figure 1C and 1E).

To better understand the kinetic mechanisms governing the conversion between cubes, THH, and RDD, we investigated the role of the chemical potential driving the etching process. By maintaining the same electron beam dose rate, the initial $FeCl_3$ concentration could be increased or decreased to modulate the chemical potential driving the system out of equilibrium. Interestingly, although both cubes and RDD etched to THH intermediate shapes (Figure 1D and 1F), cubes adopted THH with a range of different {hk0} surface facets as a function of chemical potential, while the RDD adopted a constant {hk0} THH shape with an h/k value of 2.5, regardless of chemical potential.

The underlying mechanistic reasons for why etching from {100} cubes and {110} RDD result in different THH intermediates were investigated by monitoring the progression of nanocrystal facets over time for a range of different $FeCl_3$ concentrations. Using the image analysis techniques described in the Supporting Information, the angles of the THH intermediate shapes for each frame of the videos were measured, and the corresponding {hk0} facets on the surface of the nanocrystal were calculated. When etching the cubes, the initial {100} facets of the cube rapidly become increasingly pyramid-like, indicating the creation of {hk0} facets with decreasing h/k values as the etching progressed (Figure 2A). For each cube, the facet eventually reached a steady {hk0} facet that was maintained even as the particle continued to decrease in volume (Figure 2B). The value of this steady index, and the resulting transient THH morphology, increased as the

concentration of $FeCl_3$, and the resulting chemical potential, was increased (Figure 2D). Previous in-situ etching experiments of cubes have shown {310} intermediate facets,[25] but this difference can be attributed to different chemical potentials in the etching environment. In this work, we used a higher concentration of Tris Buffer-HCl because we have observed better formation of graphene liquid cell pockets. The facet tips on the nanocyrstals can sometimes be slightly blunted, so the measured facet angle corresponds to lines drawn from the midpoint of the facet (Figure S2). In addition, the facet measurement analysis was shown to be robust to the small rotations that can be expected from diffusional motion in the graphene liquid cell (Figure S10). Although the nanocrystals were often not perfect in shape, the overall trend of higher initial $FeCl_3$ concentration leading to higher index {hk0} facets was consistent across many etched nanocubes.
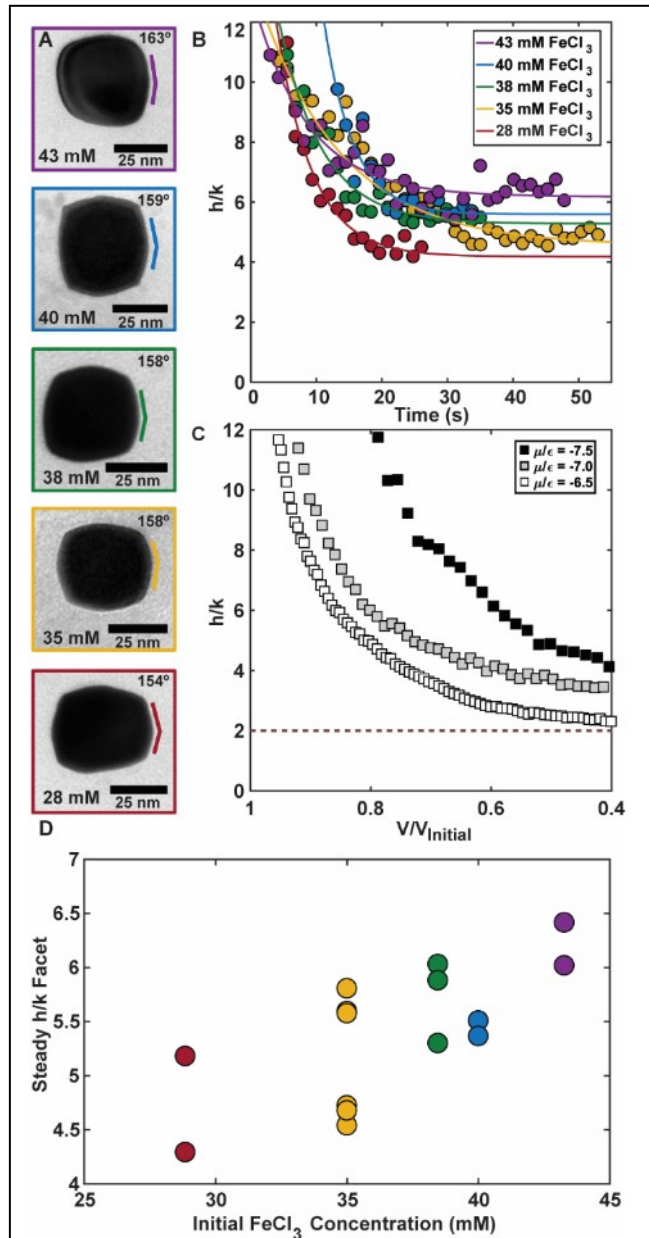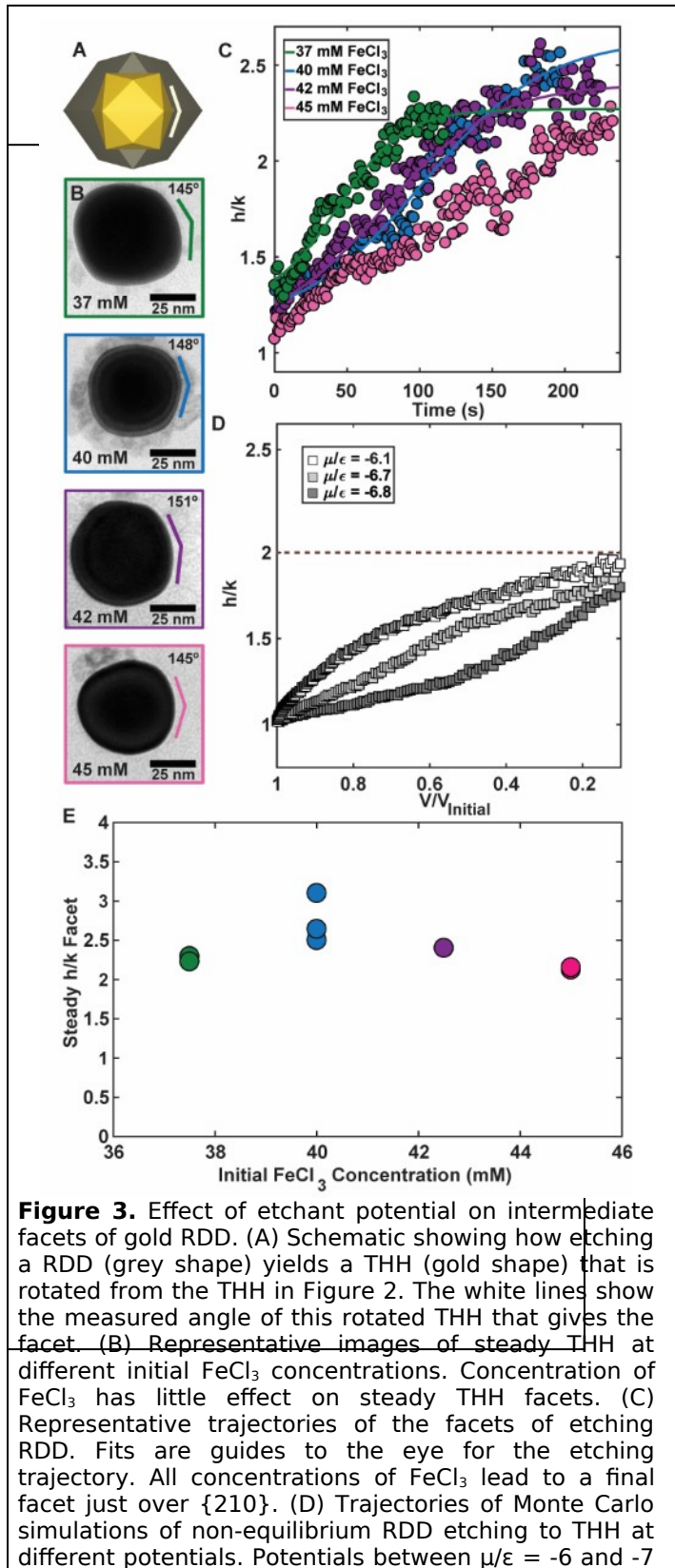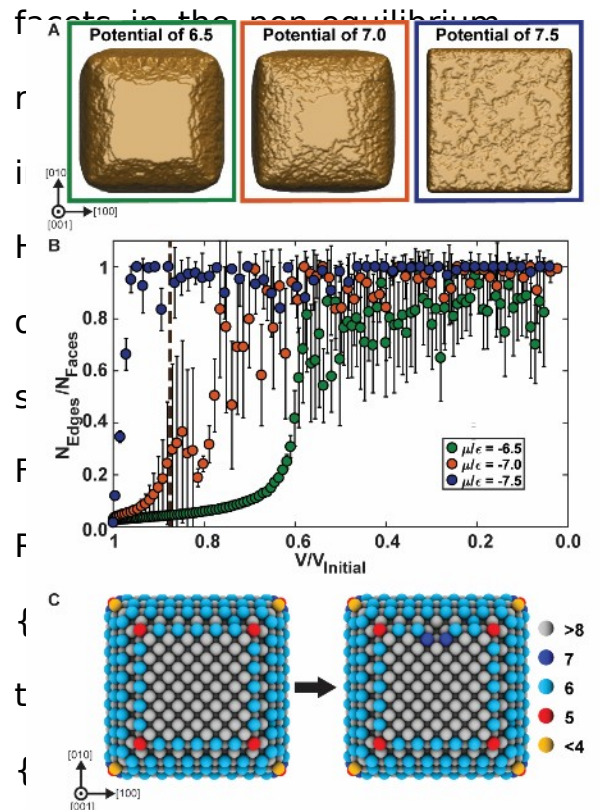
Figure 2. Effect of etchant potential on intermediate facets of gold nanocubes. (A) Representative images of intermediate THH at different initial FeCl₃ concentrations. Higher concentrations of FeCl₃ leads to higher index steady THH facets. (B) Representative trajectories of the facets of the nanocubes as they etch with colors matching concentrations in 2A. Each point is the measured facets at one frame of the etching video. Exponential fits are guides to the eye for the etching trajectories. Higher concentrations of FeCl₃ lead to higher index steady {hk0} facets. (C) Trajectories of Monte Carlo simulations of non-equilibrium etching of nanocubes to THH at different etchant

Monte Carlo simulations using a simplified, lattice-gas-like model to remove atoms from FCC cubic nanocrystals at different chemical potentials match the experimental facet trajectories and show a similar dependence of the steady {hk0} facets on driving force (Figure 2C). In the simulations, the probability (or rate) of removal of a surface atom depends on (1) its number of nearest neighbor bonds, each of which contributes an energy ε, and (2) the value of the driving force, represented in the model as a chemical potential μ. For example, at a chemical potential of μ/ε = -6.5, atoms with 6 or fewer nearest neighbor bonds are likely to be etched while atoms with 7 or more nearest neighbor bonds are not likely to be etched. Using this procedure to simulate the etching of

10

gold cubes, the initial {100} surface facet becomes steeper with the h/k value following an exponential curve qualitatively similar to the facet trajectories observed from the liquid cell TEM experiments (Figure 2C). At lower potentials, the Monte Carlo simulation shows a steeper steady {210} facet while at higher potentials the steady facet appears to level off at higher h/k facets, suggesting the concentration of $FeCl_3$ in the experiments acts as the chemical potential in the system, determining which atoms are removed. In Figure 2C, the trajectories are shown until they reach 40% of their initial volume similar to the cut-off in data for experimental particles in Figure 2B. If the simulation is continued to even smaller volumes, the facet h/k value continues decreasing even after the facet trajectory flattens out (Figure S5). The initial cubes in the liquid cell TEM experiment were potentially too small to exhibit this slow decline in h/k value after reaching the steady {hk0} facet. Regardless, the observation of different steady facets at different driving forces remains consistent. The corroboration of Monte Carlo facet trajectories with the experimental TEM facet trajectories in both shape and etchant oxidation potential dependence suggests a general mechanistic underpinning to these observations.

Figure 3. Effect of etchant potential on intermediate facets of gold RDD. (A) Schematic showing how etching a RDD (grey shape) yields a THH (gold shape) that is rotated from the THH in Figure 2. The white lines show the measured angle of this rotated THH that gives the facet. (B) Representative images of steady THH at different initial $FeCl_3$ concentrations. Concentration of $FeCl_3$ has little effect on steady THH facets. (C) Representative trajectories of the facets of etching RDD. Fits are guides to the eye for the etching trajectory. All concentrations of $FeCl_3$ lead to a final facet just over {210}. (D) Trajectories of Monte Carlo simulations of non-equilibrium RDD etching to THH at different potentials. Potentials between μ/ϵ = -6 and -7

Etching RDD particles encompassed by {110} facets in the non-equilibrium r i H c s F F { t { cubes), the intermediate THH polyhedra in Figure 3 are rotated compared to the THH shapes seen in Figure 2. Due to the rotation of the THH, only two angles can be used to measure the facets of the THH (Figure S2). Representative images of the steady THH shapes after

Figure 4. During etching of nanocubes, roughening of the edges at higher potentials leads to {hk0} facets with greater h/k values. (A) Monte Carlo simulations etching cubes at different potentials shows rougher edges on the top terraces of atoms at higher potentials. (B) Quantifying the roughness of the edges at different potentials from the Monte Carlo simulations by measuring the ratio of atoms on the edge of the nanocrystal to the number of atoms on the face. Brown line shows the time of images in (B). (C) From an atomistic perspective, where atoms are color coded by their number of nearest neighbor bonds, immediately after a 6-coordinate edge atom is removed, two

etching RDD at different concentrations of $FeCl_3$ show the rotated THH and the angles that are used for calculating facets (Figure 3B). Using the two measurable facet angles on the THH images, all the trajectories of the facets show a rise in h/k value to facets just over {210} but via different paths (Figure 3C). The nanocrystals then maintain this surface facet even as they undergo further etching. Although there are differences in the shape of the facet trajectory, multiple trials of etching RDD at varying $FeCl_3$ concentrations consistently showed a THH facet with an h/k value around 2.5.

Monte Carlo simulations on etching RDD in the non-equilibrium regime resemble reasonably well the experimental trajectories observed using graphene liquid cell TEM (Figure 3D). All of the curves with a potential between $\mu/\varepsilon = -6.1$ and $\mu/\varepsilon = -6.8$ show the facet reaching a steady asymptote around {210}. The higher potentials show a concave down facet trajectory while lower potentials show a concave up trajectory towards the {210} facet. These trajectories are qualitatively similar to the liquid cell TEM trajectories and comparing first and second derivatives of the curves shows some correlation despite noise in the experimental data (Figure S6). The remarkably close correspondence between simulation and experiment is surprising given the simplicity of the simulation model.

A closer investigation of the Monte Carlo simulations and zero temperature kinetic models can be used to rationalize the observed chemical potential

dependence of the facets during etching. Viewing each nanocube in the simulation down the [001] direction during the initial etching of the top few layers, higher driving forces show more etching into the interior of the top layer (Figure 4A). This increased removal of interior atoms leads to a roughening of the edges of the layers, which can quantitatively be shown by measuring the fraction of face atoms that are on the edge as a function of the chemical potential (Figure 4B). This edge roughness is indicative of a faster rate of removal of the top layers of atoms which will ultimately lead to flatter intermediate {hk0} facets. A color-coded, zero temperature kinetic model can explain the mechanism of this potential dependent behavior on the atomic level (Figure 4C). Starting with the top surface of a cube with {hk0} character on the edges, an edge atom can be removed if the magnitude of the chemical potential is above $\mu/\varepsilon = 6$. Immediately after removal of that 6-coordinate edge atom, two 7-coordinate inner atoms are exposed. At potentials well below a magnitude of $\mu/\varepsilon = 7$, these two newly exposed atoms cannot be removed, and etching continues removing the 6-coordinate atoms that form the square edge of the plane. At potentials close to or above magnitude $\mu/\varepsilon = 7$, these newly exposed 7-coordinate atoms become likely to be removed, leading to both a roughening of the edge and a faster removal of the top terrace of atoms. It is important to remember that removal of atoms in the Monte Carlo simulation is a probabilistic event, so adjusting the chemical potential changes the likelihood that an atom is removed. This probability of removing interior 7-coordinate atoms increases

at higher potentials, leading to the faster removal of the top layers of atoms and flatter {hk0} THH facets. Therefore, the oxidation potential controls the kinetic roughening of the edges during etching of cubes which dictates the steady state {hk0} facet on the intermediate THH shape.

Although the etching of cubes from {100} to various {hk0} THH is understandable in terms of kinetic roughening, the simulated RDD always approach a {210} THH in the non-equilibrium etching regime, regardless of chemical potential. The surface atoms of the initial {110} RDD consist primarily of 7-coordinate facet atoms with 5-coordinate edge atoms (Figure 5A). The RDD etching behavior seen in the liquid cell experiments can only be recreated in the Monte Carlo models when the potential is set such that atoms with less than 7 nearest neighbor bonds are removed (Figure S8). In that potential regime, a mechanism of etching occurs that consists of chains of atoms being removed from the {110} faces via the edges. (Figure 5A) This etching leaves behind {210} facets on the faces (see Step 11 of Figure 5B).
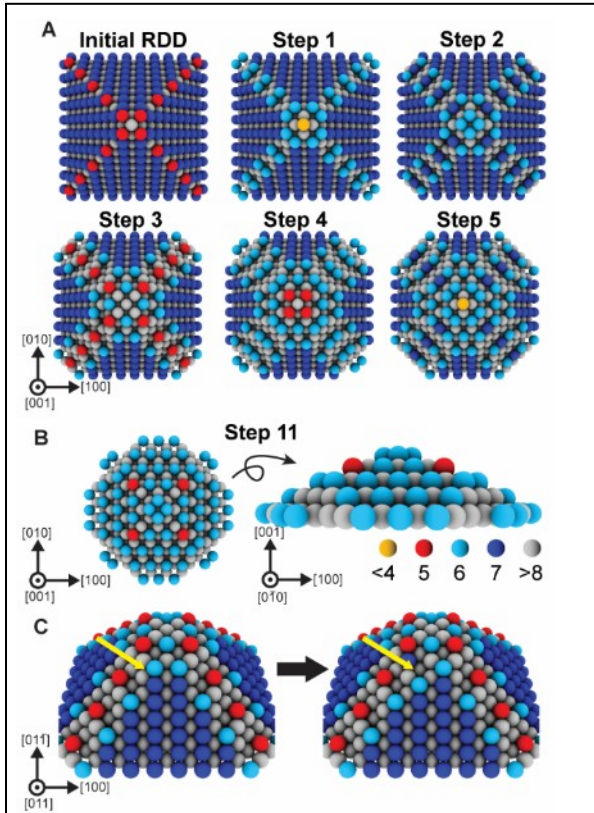
Figure 5. Atomistic model of how Monte Carlo simulations predict a final facet of {210} for etched RDD regardless of etchant potential. (A) Atoms are color-coded by the number of first nearest neighbors. In each step, atoms with less than 7 nearest neighbors are removed. (B) Removing atoms in this manner leads to {210} facets, as shown in Step 11. When viewed down the [010] direction, the {210} facet can be visually seen. (C) From an atomistic perspective, immediately when a 6-coordinate edge atom is removed, a new 6-coordinate atom is revealed. The ratio of removal probability between the edge atoms

This chain-like mechanism can also explain why the transition from {110} RDD to {210} THH does not change with the potential of the etchant. Immediately after one of the 6-coordinate atoms on the edge of the chain is removed, a new 6-coordinate interior atom is exposed (Figure 5C). Unlike in the etching of the cubes, the probability of removing the newly exposed inner atoms compared to the edge atoms does not change with potential because both atoms are 6-coordinate. Since potential does not change the likelihood of etching into the surface, the steady {hk0} facet does not vary with potential when etching from a {110} surface.

The steady facet during RDD etching does not change with potential, but the facet trajectories did have dependence on potential in both the experiment and simulation. The difference in curvature of the facet trajectories at different etchant potentials is due to the changes in the ability of atoms on the face of the {110} facet to be removed. As the etchant potential

increases, the probabilistically unlikely event of removing a 7-coordinate atom on the {110} surface becomes more common. Once a 7-coordinate surface atom gets removed, it exposes two 6-coordinate atoms, thus inducing a chain-like etching mechanism that removes all the atoms in its row (Figure S9). Higher potentials increase the probability of these unlikely events, leading to the nanocrystal maintaining the {110} character of its facets for longer times (Figure S8).

These results highlight the importance of single-particle measurements of non-equilibrium processes enabled by graphene liquid cell TEM experiments coupled with Monte Carlo simulations. Although the assumption that atoms etch based on their coordination number has been previously reported,[25,32,33] this data reveals important mechanistic understanding of how the chemical potential of a kinetically-driven reaction can be used to sculpt nanocrystals to adopt specific surface facets. This is valuable since non-equilibrium growth and etching pathways are a powerful tool to create energetically unfavorable shapes, but detailed atomic-level understanding of these processes is lacking from the literature. We envision this approach as allowing for detailed mapping of the energy landscape of various inorganic nanocrystal systems, facilitating the rational synthesis of faceted nanocrystals for specific applications.

ASSOCIATED CONTENT

Supporting Information

The Supporting Information is available free of charge on the ACS Publications website at DOI: XXX

The experimental methods including nanoparticle synthesis, graphene liquid cell fabrication, TEM imaging conditions, and simulation methods are described. Additional figures include image analysis techniques and measurement methods. Additional zero temperature kinetic models and Monte Carlo simulations are also shown. The Matlab code for analyzing frames of the TEM video are presented.

Supplementary videos of cubes and rhombadodecahedra etching are also available.

Data Availability

The raw TEM data presented are available on the DASH repository at DOI 10.6078/D14H46.

AUTHOR INFORMATION

Corresponding Author

*E-mail: paul.alivisatos@berkeley.edu

ORCID

Matthew R. Hauwiller: 0000-0002-5448-6937

Layne B. Frechette: 0000-0002-4263-6651

Matthew R. Jones: 0000-0002-9289-291X

Justin C. Ondry: 0000-0001-9113-3420

Grant M. Rotskoff

Phillip Geissler

A. Paul Alivisatos: 0000-0001-6895-9048

Notes

Any additional relevant notes should be placed here.

ABBREVIATIONS

TEM, Transmission electron microscope; RDD, rhombic dodecahedra; THH, tetrahexahedra.

REFERENCES

(1)   Lu, X.; Rycenga, M.; Skrabalak, S. E.; Wiley, B.; Xia, Y. *Annu. Rev. Phys. Chem.* **2009**, *60*, 167–192.

(2) Dreaden, E. C.; Alkilany, A. M.; Huang, X.; Murphy, C. J.; El-Sayed, M. A. *Chem. Soc. Rev.* **2012**, *41*, 2740–2779.

(3) Jing, H.; Zhang, Q.; Large, N.; Yu, C.; Blom, D. A.; Nordlander, P.; Wang, H. *Nano Lett.* **2014**, *14*, 3674–3682.

(4) Narayanan, R.; El-Sayed, M. A. *Nano Lett.* **2004**, *4*, 1343–1348.

(5) Huang, X.; El-Sayed, I. H.; Qian, W.; El-Sayed, M. A. *J. Am. Chem. Soc.* **2006**, *128*, 2115–2120.

(6) Huang, X.; El-Sayed, M. A. *Alexandria J. Med.* **2011**, *47*, 1–9.

(7) Khosla, K.; Wang, Y.; Hagedorn, M.; Qin, Z.; Bischof, J. *ACS Nano* **2017**, acsnano.7b02216.

(8) Marks, L. D.; Peng, L. *J. Phys. Condens. Matter* **2016**, *28*, 053001.

(9) Xia, X.; Zeng, J.; McDearmon, B.; Zheng, Y.; Li, Q.; Xia, Y. *Angew. Chemie - Int. Ed.* **2011**, *50*, 12542–12546.

(10) Quan, Z.; Wang, Y.; Fang, J. *Acc. Chem. Res.* **2013**, *46*, 191–202.

(11) Zhou, K.; Li, Y. *Angew. Chemie Int. Ed.* **2012**, *51*, 602–613.

(12) Zhou, Z.-Y.; Tian, N.; Li, J.-T.; Broadwell, I.; Sun, S.-G. *Chem. Soc. Rev.* **2011**, *40*, 4167.

(13) Zheng, H.; Smith, R. K.; Jun, Y.; Kisielowski, C.; Dahmen, U.; Alivisatos, A. P. *Science* **2009**, *324*, 1309–1312.

(14) Liao, H.-G.; Cui, L.; Whitelam, S.; Zheng, H. *Science* **2012**, *336*, 1011–1014.

(15) Li, D.; Nielsen, M. H.; Lee, J. R. I.; Frandsen, C.; Banfield, J. F.; De Yoreo, J. J. *Science* **2012**, *336*, 1014–1018.

(16) Ross, F. M. *Science* **2015**, *350*, aaa9886-aaa9886.

(17) Zhu, C.; Liang, S.; Song, E.; Zhou, Y.; Wang, W.; Shan, F.; Shi, Y.; Hao, C.; Yin, K.; Zhang, T.; et al. *Nat. Commun.* **2018**, *9*, 1–7.

(18) Yuk, J. M.; Park, J.; Ercius, P.; Kim, K.; Hellebusch, D. J.; Crommie, M. F.; Lee, J. Y.; Zettl, A.; Alivisatos, A. P. *Science* **2012**, *336*, 61–64.

(19) Jeong, M.; Yuk, J. M.; Lee, J. Y. *Chem. Mater.* **2015**, 3200–3202.

(20) Park, J.; Elmlund, H.; Ercius, P.; Yuk, J. M.; Limmer, D. T.; Chen, Q.; Kim, K.; Han, S. H.; Weitz, D. A.; Zettl, A.; et al. *Science* **2015**, *349*, 290–295.

(21) Hauwiller, M. R.; Ondry, J. C.; Alivisatos, A. P. *J. Vis. Exp.* **2018**, No. 135, 1–9.

(22) Jiang, Y.; Zhu, G.; Lin, F.; Zhang, H.; Jin, C.; Yuan, J.; Yang, D.; Zhang, Z. *Nano Lett.* **2014**, *14*, 3761–3765.

(23) Jiang, Y.; Zhu, G.; Dong, G.; Lin, F.; Zhang, H.; Yuan, J.; Zhang, Z.; Jin, C. *Micron* **2017**, *97*, 22–28.

(24) Wu, J.; Gao, W.; Yang, H.; Zuo, J.-M. *ACS Nano* **2017**, *11*, 1696–1703.

(25) Ye, X.; Jones, M. R.; Frechette, L. B.; Chen, Q.; Powers, A. S.; Ercius, P.; Dunn, G.; Rotskoff, G. M.; Nguyen, S. C.; Adiga, V. P.; et al. *Science* **2016**, *354*, 874–877.

(26) O'Brien, M. N.; Jones, M. R.; Brown, K. A.; Mirkin, C. A. *J. Am. Chem. Soc.* **2014**, *136*, 7603–7606.

(27) Schneider, N. M.; Norton, M. M.; Mendel, B. J.; Grogan, J. M.; Frances, M.; Bau, H. H. *J. Phys. Chem. C* **2014**, *118*, 22373–22382.

(28) Park, J. H.; Schneider, N. M.; Grogan, J. M.; Reuter, M. C.; Bau, H. H.; Kodambaka, S.; Ross, F. M. *Nano Lett.* **2015**, *15*, 5314–5320.

(29) Zou, R.; Guo, X.; Yang, J.; Li, D.; Peng, F.; Zhang, L.; Wang, H.; Yu, H. *CrystEngComm* **2009**, *11*, 2797.

(30) Ma, Y.; Li, W.; Zeng, J.; McKiernan, M.; Xie, Z.; Xia, Y. *J. Mater. Chem.* **2010**, *20*, 3586.

(31) Long, R.; Zhou, S.; Wiley, B. J.; Xiong, Y. *Chem. Soc. Rev.* **2014**, *43*, 6288.

(32) Ruditskiy, A.; Xia, Y. *ACS Nano* **2017**, *11*, 23–27.

(33) Ruditskiy, A.; Vara, M.; Huang, H.; Xia, Y. *Chem. Mater.* **2017**, *29*, 5394–5400.